Applied Surface Science 556 (2021) 149664

Contents lists available at ScienceDirect

Applied Surface Science

journal homepage: www.elsevier.com/locate/apsusc

Defective impacts on amorphous $WO_3 \cdot H_2O$ films using accelerated hydrolysis effects for flexible electrochromic energy-storage devices

Myeong-Hun Jo [a,1], Bon-Ryul Koo [b,1], Hyo-Jin Ahn [a,b,*]

[a] Department of Materials Science and Engineering, Seoul National University of Science and Technology, Seoul 01811, South Korea
[b] Program of Materials Science & Engineering, Convergence Institute of Biomedical Engineering and Biomaterials, Seoul National University of Science and Technology, Seoul 01811, South Korea

ARTICLE INFO

Keywords:
Amorphous $WO_3 \cdot H_2O$
Hydrolysis
Low-temperature process
Flexible film
Electrochromic energy-storage performances

ABSTRACT

We newly developed amorphous $WO_3 \cdot H_2O$ (a-$WO_3 \cdot H_2O$) films with porosity and oxygen vacancy (V_O) defects through a humidity adjustment causing the accelerated hydrolysis of $WOCl_4$ with H_2O during spin-coating and during low-temperature annealing for flexible electrochromic (EC) energy-storage devices. Optimizing the hydrolysis effect in all a-$WO_3 \cdot H_2O$ films, we adjusted the humidity to 25, 35, and 45% in a humid chamber. Specifically, the a-$WO_3 \cdot H_2O$ film fabricated at 35% exhibited a developed porous morphology and an increased number of V_O defects, providing increased electrochemically active sites and enhanced electrical conductivity, respectively, due to the accelerated hydrolysis of $WOCl_4$ and the increased intercalation of water molecules. Such behaviors of the a-$WO_3 \cdot H_2O$ film bring about superior flexible EC energy-storage performances of widened transmittance modulation (60.0% at 633 nm), fast switching speeds (3.4 s for coloration speed and 4.2 s for bleaching speed), a high CE (62.7 cm^2/C), good specific capacitance (94.2 F/g at 2 A/g), and rate capability (74.3%). Specifically, the increased transmittance modulation and specific capacitance stem from the increased electrochemical activity caused by the enriched electrochemically active sites. Moreover, the fast switching speeds and good rate capability are generated by electrochemical kinetics improved with the porous morphology and the increased V_O.

1. Introduction

With the advent of global issues such as resource exhaustion and environmental pollution, the development of energy-efficient devices such as smart windows, electrochemical capacitors, and lithium-ion batteries has been progressing rapidly [1-3]. Specifically, smart windows, which can save more than 40% of otherwise wasted energy, are regarded as a superior energy-saving application given how they can adjust the sunlight influx by controlling the optical properties based on electrochromic (EC) reactions [4]. Typically, the color change of an EC device is generated by the insertion/extraction of Li ions and electrons accompanying pseudocapacitive energy-storage. Thus, EC devices can provide color variations together with an energy-storage function, capabilities that expand their applications to areas such as EC supercapacitors and EC batteries in the form of EC energy-storage devices [5-7]. Despite the multi-functionality of EC energy-storage devices, more functions and novel aspects are being explored to widen their application areas [8-10]. For instance, bendable and wearable EC devices that meet flexible requirements have been developed for possible application in EC e-skins, soft displays, and portable electronics [11]. In this streaming, several studies which are mainly focused on flexible transparent electrode and deposition technique for EC films have been conducted to develop flexible multi-functional EC devices by research groups. For example, Mai's group firstly developed Ag nanowires/WO_3 hybrid films for the flexible electrochromic supercapacitors [12]. Also, Lee's group realized high-quality patterns by direct inkjet-patterning WO_3-PEDOT:PSS composites on the substrates for flexible EC devices [13]. However, to the best of our knowledge, development of EC material itself and structural modeling, which are directly involved in the device performance has not been considered sufficient.

In general, EC energy-storage devices have a sandwich structure with transparent conducting layer/cathodic material/electrolyte/anodic

* Corresponding author at: Department of Materials Science and Engineering, Seoul National University of Science and Technology, Seoul 01811, South Korea (H.-J. Ahn).
E-mail address: hjahn@seoultech.ac.kr (H.-J. Ahn).
[1] M.-H. Jo and B.-R. Koo contributed equally to this work.

https://doi.org/10.1016/j.apsusc.2021.149664
Received 28 December 2020; Received in revised form 25 February 2021; Accepted 24 March 2021
Available online 8 April 2021
0169-4332/© 2021 Elsevier B.V. All rights reserved.

material/transparent conducting layer [14]. The EC energy-storage performances (transmittance modulation, switching speeds, coloration efficiency (CE), specific capacitance, and rate capability) are mainly dominated by the electrochemical reactions in the active layers of the cathodic and anodic materials [4,8]. Typically, the transmittance modulation, CE, and specific capacitance are affected by the electrochemical activity of the active layers related to the insertion/extraction of Li ions and electrons under the applied voltage [15,16]. The switching speeds and the rate capability are influenced by the electrochemical kinetics related to the Li ion diffusivity and electrical conductivity of the active layers [17,18]. Representative active materials for EC energy-storage devices such as Prussian blue, viologens, and WO_3, have been studied to improve their performances [19,20]. Among them, WO_3 is considered as a promising candidate for the cathodic material due to its superior transmittance modulation, high CE, capacitance, and long cycle stability via a renovated morphology and heteroatom doping. For example, Zhang *et al.* developed macroporous WO_3 with enhanced an active surface area by anodic oxidation of DC-sputtered tungsten layers at 400 °C, resulting in high optical transmittance (50.0% at 632.8 nm) and high CE (58 cm^2/C) [21]. Also, Zhou et al. reported a Mo-doped WO_3 nanowire array via spin-coating and a hydrothermal method at 400 °C and 190 °C, respectively, resulting in significant optical modulation (56.7% at 750 nm), improved discharge capacity (48.67 mA h g^{-1} at 2 A g^{-1}), and good cycling stability (38.2% at 4 A g^{-1} for 5500 cycles) [22]. Each renovated WO_3 sample exhibiting superb EC energy-storage properties was synthesized under a high temperature annealing process (>300 °C) to provide sufficient energy for pore development and doping. However, to realize flexible WO_3 films, a process with a high annealing temperature can induce the critical deformation of polymeric substrates such as polyethylene terephthalate (PET), polyethylene naphthalate (PEN), and polycarbonate (PC), making this process inappropriate for flexible EC energy-storage devices [23,24]. In relation to this, Xiao *et al.* fabricated WO_3 nanocolumns with porous surface features that exhibited excellent flexible EC properties via electron beam deposition on ITO/PET [25]. Also, Ji et al. reported flexible nanoporous WO_{3-x} films via a combined process of DC sputtering and anodizing on ITO/PET [10]. However, most studies to realize flexible WO_3 films on polymeric substrates have been conducted via high-energy deposition techniques, which are expensive, unfavorable for large scales, and difficult with regard to thickness control [26,27]. Thus, to realize flexible WO_3 films with superior properties through a low-temperature process for advanced flexible EC energy-storage devices, further studies are needed. However, there are few reports concerning flexible WO_3 films fabricated at a low temperature using hydrolysis effects without high-energy deposition techniques.

Hydrated phase of WO_3 ($WO_3{\cdot}H_2O$) is valuable for upgrading its physical and electrochemical behaviors during ion insertion/extraction. The intercalated water molecules in crystalline structure can form infinite two-dimensional layered structure with expanded gaps between the stacks, leading to rapid diffusion of proton or alkali ion and improving ionic storage ability [28]. This effect can also make them stabilized during violent electrochemical reactions by corner sharing [WO_6] octahedral with water molecules [29]. In addition, the effort to induce various defects such as oxygen vacancy, frank disorder, and stacking fault into $WO_3{\cdot}H_2O$ can be potential strategy for accelerating the redox performances and even gas sensing and photocatalytic abilities [30]. The frank disorder and stacking fault have a strong effect in relaxing the stress and electrostatic repulsion in the structures, which can be effective to reduce diffusion barriers or migration energy of protons and alkali ions [31]. Also, forming oxygen vacancies in $WO_3{\cdot}H_2O$ can be related to increasing electron density to improve electrical and electrochemical performances [32]. Therefore, realizing defective impact on $WO_3{\cdot}H_2O$ should be reasonable study to be developed for high-performance flexible EC energy-storage devices.

In this study, we invented amorphous $WO_3{\cdot}H_2O$ (a-$WO_3{\cdot}H_2O$) films with porosity and oxygen vacancy (V_O) defects via accelerated hydrolysis effects during spin-coating and low temperature annealing (80 °C) to realize flexible EC energy-storage devices. The porous morphology and V_O of the a-$WO_3{\cdot}H_2O$ films stem from the optimized hydrolysis of $WOCl_4$, which is highly reactive to H_2O leading to enhanced electrochemical activity and kinetics. The a-$WO_3{\cdot}H_2O$ films given their porosity and V_O properties exhibited superior EC energy-storage performances such as a wide range of transmittance modulation, fast switching speeds, high CE, and good specific capacitance and rate capability outcomes.

2. Experimental details

The a-$WO_3{\cdot}H_2O$ films used here were prepared by the hydrolysis of $WOCl_4$ molecules given their high reactivity to H_2O in a humid chamber during a spin-coating process, with a subsequent low-temperature (80 °C) annealing step. Before the spin-coating process, commercial PEN substrates coated with indium tin oxide (ITO, 15 Ω/□) were successively cleaned in acetone by means of ultrasonication. The WCl_6 solution used for spin-coating containing $WOCl_4$ molecules induced from the dynamic chemical reaction between the solute and the solvent was prepared by dissolving 10 wt% tungsten chloride (WCl_6, Aldrich) as a solute into 2-propanol ($(CH_3)_2CHOH$, Aldrich) as a solvent. After vigorous stirring, each transparent blue WCl_6 solution was spin-coated two times on flexible PEN substrates at a speed of 2000 rpm for 30 s in a chamber adjusted to humidity levels of 25%, 35%, and 45%, a process which leads to the formation of flexible a-$WO_3{\cdot}H_2O$ films (hereafter termed as the a-$WO_3{\cdot}H_2O$/25%, a-$WO_3{\cdot}H_2O$/35%, and a-$WO_3{\cdot}H_2O$/45% samples). Thereafter, all of the flexible a-$WO_3{\cdot}H_2O$ films were annealed at 80 °C for 1hr for the successful removal of residual organics.

To realize the surface morphologies of all of the film samples, field-emission scanning electron microscopy (FESEM, Hitachi S–4800) was carried out. For the investigation of the film structure and chemical bonding state, X-ray diffraction measurements (XRD, Rigaku D/Max–2500, Cu Kα radiation) and X-ray photoelectron spectroscopy measurements (XPS, ESCALAB 250, Al Kα radiation) were conducted, respectively. The optical and electrical properties were correspondingly identified via ultraviolet-visible (UV-vis) spectroscopy (PerkinElmer, Lambda 35) and a Hall-effect measurement system (Ecopia, HMS–3000).

The flexible EC performances of all of the a-$WO_3{\cdot}H_2O$ here films were characterized through a combination of UV-vis spectroscopy and potentiostat/galvanostat (PGSTAT302N, Metrohm Autolab). The electrochemical analysis and energy-storage performance tests were carried out using potentiostat/galvanostat. The EC energy-storage performances of the a-$WO_3{\cdot}H_2O$ films were assessed in a three-electrode system consisting of a-$WO_3{\cdot}H_2O$ films as the working electrode, Ag wire as the reference electrode, Pt wire as the counter electrode, and 1 M of $LiClO_4$ (Aldrich) in propylene carbonate (PC, $C_4H_6O_3$, Aldrich) as the electrolyte. To derive the Li ion diffusion coefficients of all of the a-$WO_3{\cdot}H_2O$ films, the scan rates (0.5, 1.0, 1.5, and 2.0 mV/s) were controlled gradually during the cyclic voltammetry step. The cycling stability test was evaluated by consecutive coloration-bleaching (each step maintained for 30 s at –0.7 V for coloration and 0.3 V for bleaching). The flexible solid-state cell was assembled with a-$WO_3{\cdot}H_2O$/35% film as a working electrode, $H_2PtCl_6{\cdot}6H_2O$ (Aldrich) film in terpineol (Aldrich) as a counter electrode, and $LiClO_4$/PMMA/PC-based gel polymer electrolyte. The bending test of the flexible solid-state cell was conducted using as all-electric dynamic test instrument (E3000, ElectroPuls^{TM}).

3. Results and discussion

Fig. 1 shows FESEM images (Fig. 1a–c for the top-view and Fig. 1d–f for the side-view) of the flexible a-$WO_3{\cdot}H_2O$ films prepared at three different humidity levels. In Fig. 1a and d, the a-$WO_3{\cdot}H_2O$/25% shows homogeneous film surface with a thickness in the range of 190.9–212.7 nm, which can be derived through the hydrolysis of $WOCl_4$ with the

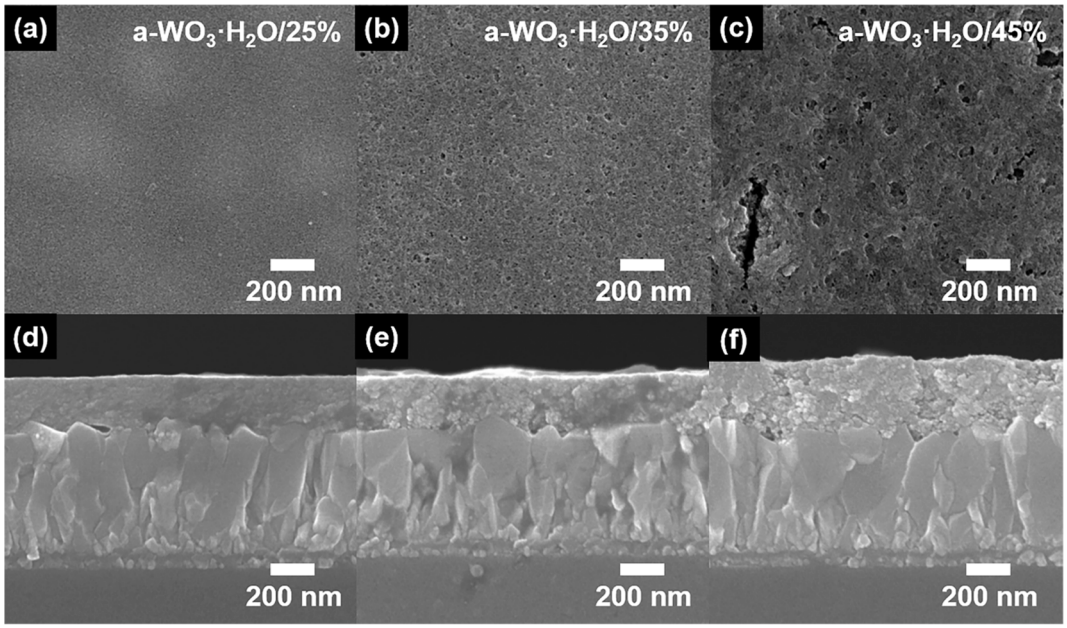

Fig. 1. Top-view and side-view FESEM images of films with different humidity levels: (a and d) a-WO_3·H_2O/25%, (b and e) a-WO_3·H_2O/35%, and (c and f) a-WO_3·H_2O/45%

reaction of H_2O molecules during the spin-coating process onto the flexible ITO PEN substrate. The $WOCl_4$ molecules originated from the vigorous reactions between WCl_6 as the solute and C_3H_8O as the solvent in the solution used for spin-coating (see *Eqs.* (1) and (2)), possibly serving as a trigger for the strong chemical reaction with H_2O molecules and resulting in a-WO_3·H_2O through spin-coating following the low-temperature annealing process at 80 °C (see *Eq.* (3)) [33-35].

$$WCl_6 + nC_3H_8O \rightarrow W(OC_3H_7)_nCl_{6-n} + nHCl \quad (1)$$

$$W(OC_3H_7)Cl \rightarrow WOCl_4 + C_3H_7Cl \quad (2)$$

$$WOCl_4 + 3H_2O \rightarrow WO_3 \cdot H_2O + 4HCl \quad (3)$$

As the relative humidity increases to 35%, the porous film surface of a-WO_3·H_2O/35% tends to form (Fig. 1b and e), together with increased film thickness levels (216.5–240.2 nm) compared to a-WO_3·H_2O/25%. This outcome can be attributed to the increased number of H_2O molecules that accelerate the hydrolysis of $WOCl_4$, which is increasing nucleation and aggregation rates of amorphous WO_3·H_2O clusters [36-38]. The accelerated aggregation of WO_3·H_2O amorphous clusters subsequently can form granules which is leading to the porous structure of a-WO_3·H_2O/35% film as confirmed in SEM images (see Fig. 1b and e)

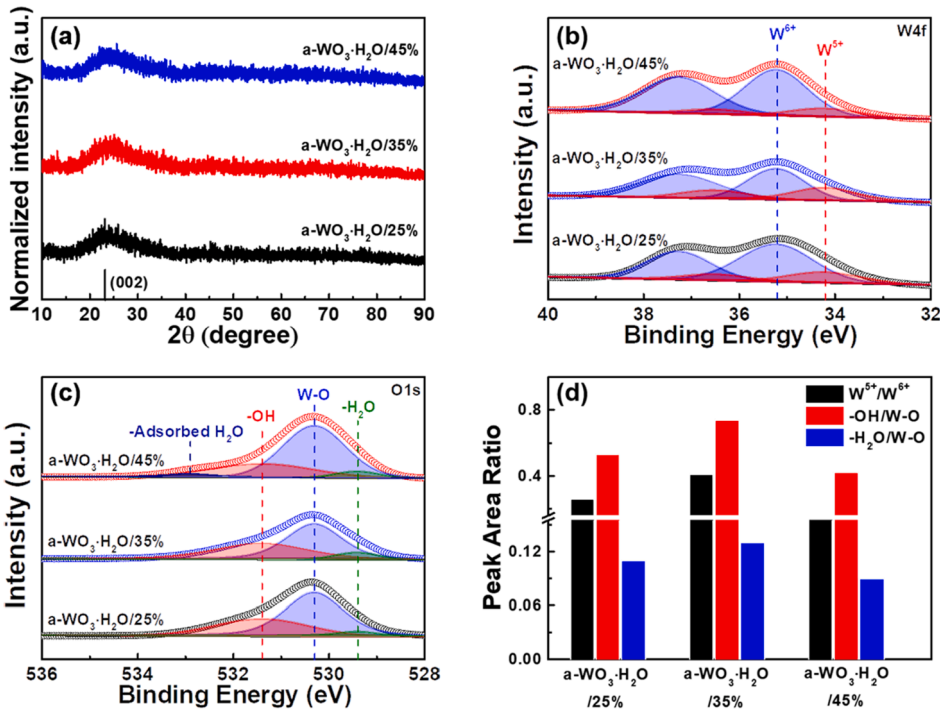

Fig. 2. (a) XRD curves and XPS spectra of the (b) W 4*f*, (c) O 1*s*, and (d) peak area ratios of W^{5+}/W^{6+}, —OH/W-O, and —H_2O/W-O obtained from all films.

[39,40]. However, when the relative humidity increases to 45%, cracks form on the film surface due to the serious aggregations and thicker film structure (329.7–363.1 nm) induced by the excessive hydrolysis (see Fig. 1c and f), deteriorating the charge transport at the active film during the electrochemical reactions [41,42]. Therefore, the optimized porous film morphology of a-WO_3·H_2O/35% can provide improved electrochemical active sites and efficient charge transport, making this combination useful for transmittance modulation and feasible specific capacitance levels of flexible EC-energy storage devices.

To identify the structure and chemical bonding states of all of the flexible a-WO_3·H_2O films, XRD and XPS analyses were conducted. The XRD patterns of all a-WO_3·H_2O films feature broad peaks centered at 23.1°, which indicate the successful formation of an amorphous structure of the type desirable for good EC energy-storage performances owing to the corresponding loose structure, facilitating efficient Li ions diffusion (see Fig. 2a) [43]. For the W 4*f* XPS spectra, all of the a-WO_3·H_2O films equally exhibit two major peaks comprising the characteristic intensity levels at ~35.2 eV of W $4f_{7/2}$ and ~37.2 eV of the W $4f_{5/2}$ peaks, in agreement with the binding energy of W^{6+} and related to the proof of the formation of the WO_3 phase. In addition, the extra minor peaks at ~34.2 eV of W $4f_{7/2}$ and ~36.5 eV of W $4f_{5/2}$ are evidence of W^{5+}, indicating the generation of V_O in the a-WO_3-based films [31,43]. Hence, the peak ratio of W^{5+}/W^{6+} in the XPS W 4*f* spectra, —OH/W-O, and the —H_2O/W-O in O 1s spectra is observed to be improved with an increase of the humidity to 35%, stemming from the accelerated intercalation of water molecules. The increased intercalation of water molecules capable of stabilizing the oxygen deficient structure through H_2O—W^{5+} bond (2.37 Å) similar in length to W—O bond (2.38 Å) results in abundant V_O providing extra electrons and efficient charge transport channels [44,45]. However, for the a-WO_3·H_2O/45% with the decreased peak ratios of —OH/W-O (0.42) and —H_2O/W-O (0.09), H_2O was adsorbed on saturated —OH due to excessive hydrolysis, as confirmed by the strong emission of the adsorbed H_2O peak at 532.9 eV (see Fig. 2c and d) [46]. Therefore, the optimized hydrolysis effects of a-WO_3·H_2O/35% with the abundant V_O, which act as donors and provide favorable electron pathways, can accelerate the switching speeds of flexible EC energy-storage devices.

Fig. 3a and b show the electrical and optical properties of all of the a-WO_3·H_2O films. The a-WO_3·H_2O/35% shows increased electrical conductivity of 2.68×10^{-4} S/cm compared to the a-WO_3·H_2O/25% (1.35×10^{-4} S/cm), which likely results from the improved carrier concentration and mobility (see Fig. 3a). The increased carrier concentration and Hall mobility stem from the abundant V_O, leading to donors and efficient charge transport channels, respectively, generated from the increased intercalation of water molecules [47]. In contrast, the a-WO_3·H_2O/45% exhibited diminished electrical conductivity (5.60×10^{-5} S/cm) related to the decreased carrier concentration and mobility. The decreased carrier concentration is mainly derived from the deficient V_O, while the decreased Hall mobility is mainly affected by the discontinuous film with cracks (see Table S1) [48]. In Fig. 3b, Tauc plots obtained from the absorbance *vs* wavelength curve were established to find out the bandgap energy levels of all a-WO_3·H_2O films. The variation affecting the optical bandgap energy (E_g) of the films was calculated according to the relationship between $(\alpha h\nu)^2$ and the photon energy ($h\nu$), as follows in *Eq.* (4) [4,14]:

$$(\alpha h\nu)^{1/n} = A(h\nu - E_g) \tag{4}$$

where α is the absorption coefficient, n is the transition type, and A is a constant. Here, E_g can be obtained by fitting the linear region by extrapolating each curve to the x-axis (see the dotted lines in Fig. 3b). The a-WO_3·H_2O/25% and a-WO_3·H_2O/35% exhibit bandgap energy levels of 3.10 eV and 3.03 eV, respectively, in agreement with the values of amorphous WO_3 according to previous reports [49,50], proving the successful formation of transparent a-WO_3·H_2O films for EC energy-

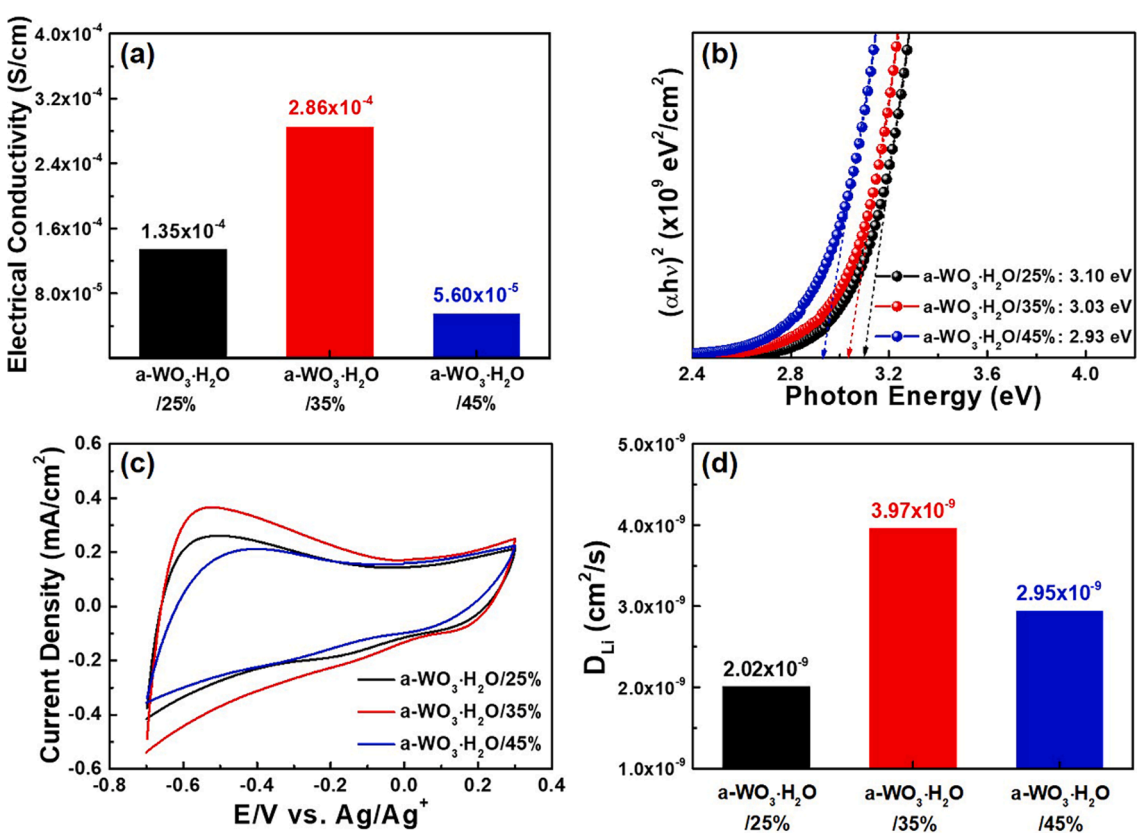

Fig. 3. (a) Electrical conductivity, (b) bandgap energy, (c) CV curves measured from −0.7 V to 0.3 V at a scan rate of 20 mV/s, and (d) Li ion diffusion coefficients calculated from the Randles–Sevcik equation of all films.

storage devices (see Fig. S1). The bandgap narrowing from a-$WO_3 \cdot H_2O$/25% to a-$WO_3 \cdot H_2O$/35% is generated by the enhanced V_O resulting in impurity states [51]. As the humidity accelerates to 45%, there is a further bandgap narrowing (2.93 eV) compared to the other films. This bandgap narrowing is generated by the adsorbed H_2O, which form impurity states above the valance band [52]. Therefore, the optimized hydrolysis effects producing abundant V_O in a-$WO_3 \cdot H_2O$/35% exhibit superior electrical conductivity, which can have an impact on the electrochemical kinetics in relation to the fast switching speeds and good rate capability of flexible EC energy-storage devices.

Fig. 3c shows the CV curves of all of the a-$WO_3 \cdot H_2O$ films in a voltage range from −0.7 to 0.3 V at a 20 mV/s scan rate. All of the a-$WO_3 \cdot H_2O$ films display a broad redox curve without specific sharp peaks related to the electrochemical behavior of amorphous WO_3 previously reported in the literature [8,17], and the reversible redox reaction involving the insertion/extraction of Li ions and electrons produces a color change from the deep blue Li_xWO_3 to the transparent WO_3. The redox reaction in the a-$WO_3 \cdot H_2O$ films can be expressed as follows by *Eq.* (5) [14,15]:

$$WO_3(\text{bleached}) + xLi^+ + xe^- \leftrightarrow Li_xWO_3(\text{colored}) \quad (5)$$

The increase of the CV curve area from a-$WO_3 \cdot H_2O$/25% to a-$WO_3 \cdot H_2O$/35% throughout the applied potential stems from the enhanced electrochemical activity to produce the increased insertion/extraction of Li ions and electrons by the porous film surface, functioning as improved electrochemical active sites. However, the a-$WO_3 \cdot H_2O$/45% shows a smaller CV curve area than the a-$WO_3 \cdot H_2O$/25% as a result of the diminished electrochemically active sites induced by extreme cracks, as shown in the SEM images, which interrupt the redox reaction at the electrodes (see Fig. 3c). Moreover, the optimized a-$WO_3 \cdot H_2O$/35% demonstrates superior electrochemical kinetics of Li ion diffusion, as shown in Fig. 3d. Fig. 3d shows the Li ion diffusion coefficients of all of the a-$WO_3 \cdot H_2O$ films during the EC reaction through CV measurements taken at various scan rates of 0.5, 1.0, 1.5, and 2.0 mV/s (see Fig. S3). The Randles–Sevcik equation was used to calculate the Li ion diffusion coefficient while considering the variation of the peak current density, as explained below in *Eq.* (6) [8]:

$$J_p = 2.72 \times 10^5 \times D^{1/2} \times C_0 \times v^{1/2} \quad (6)$$

where the J_p is the peak current density, the C_o is the active ion concentration of the electrolyte, and the v is the scan rate of the CV curve. The Li ion diffusion coefficient was enhanced from 2.02 × 10^{-9} cm^2/s for a-$WO_3 \cdot H_2O$/25% to 3.97 × 10^{-9} cm^2/s for a-$WO_3 \cdot H_2O$/35%, resulting from the synergistic effect between the improved electrical conductivity induced by the abundant V_O and the shortened Li ion diffusion length as the result of the porous film morphology [4,15]. However, the a-$WO_3 \cdot H_2O$/45% exhibits a lower Li ion diffusion coefficient (2.95 × 10^{-9} cm^2/s) compared to a-$WO_3 \cdot H_2O$/35% due to the inferior electrical conductivity and the extreme cracks, leading to reduced Li ion and electron transport rates [17].

Fig. 4a displays the *in-situ* transmittance curves at λ_{633nm} of all of the a-$WO_3 \cdot H_2O$ films acquired through double-step chronoamperometry (CA) measurements at the potentials of –0.7 V (colored state) and 0.3 V (bleached state) for 60 s of the repeated cycling. As described in Table 1, the a-$WO_3 \cdot H_2O$/25% film shows transmittance modulation ($\triangle T = T_b - T_c$, where T_b is the transmittance in the bleached state and T_c is the transmittance in the colored state) of 50.4% and switching speeds (the time required to reach 90% of the full transmittance modulation of the film with an area of 3.4 cm^2) of 6.4 s for the coloration speed and 8.7 s for the bleaching speed, which indicates their applicability to the flexible EC energy-storage devices. Moreover, with the optimized hydrolysis effects, a-$WO_3 \cdot H_2O$/35% film exhibits widened transmittance modulation of 60.0% and faster switching speeds of 3.4 s for the coloration speed and 4.2 s for the bleaching speed, caused by the improved electrochemical activity and kinetics, respectively. The increased electrochemical activity is generated from the porous film morphology, providing an expanded number of electrochemically active sites for the EC reaction. The resulted widening of the transmittance modulation in

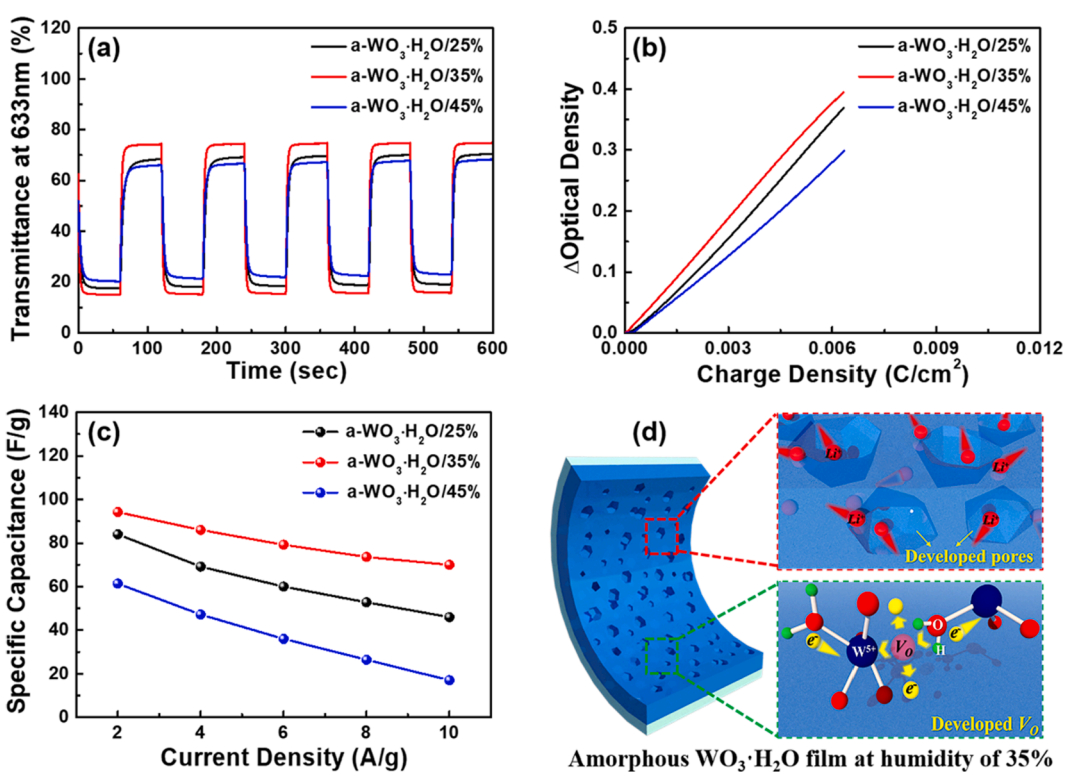

Fig. 4. (a) *In situ* optical transmittances curves applied to different potential of –0.7 V for colored states and 0.3 V for bleached states for 60 s per process, (b) optical density curves at 633 nm in response to the inserted charge density, (c) specific capacitance at given current densities of 2, 4, 6, 8, and 10 A/g obtained from all films, and (d) schematic illustration of the Li ions and electrons transport mechanisms with the developed pores and oxygen vacancies of a-$WO_3 \cdot H_2O$/35% film.

Table 1
Summary of the EC energy-storage performances of all samples.

	Transmittance modulation (%, 633 nm)	Coloration speed (s)	Bleaching speed (s)	CE (cm^2/C)	Specific Capacitance (F/g, at 2 A/g)
a-$WO_3 \cdot H_2O$/25%	50.4	6.4	8.7	54.6	84.0
a-$WO_3 \cdot H_2O$/35%	60.0	3.4	4.2	62.7	94.2
a-$WO_3 \cdot H_2O$/45%	44.8	6.7	7.0	50.1	61.4

a-$WO_3 \cdot H_2O$/35% compared to the other samples is also confirmed by the optical transmittance curves in a wavelength range of 400–900 nm with the photographs of the flexible a-$WO_3 \cdot H_2O$/35% film in colored state (−0.7 V) and bleached state (0.3 V) (see Fig. S2). The enhanced electrochemical kinetics is closely associated with the increased Li ion diffusion coefficient and electrical conductivity resulting from the porous surface and the abundant V_O. However, the a-$WO_3 \cdot H_2O$/45% displays a reduced level of transmittance modulation of 44.8% stemming from the inferior electrochemical activity caused by the fewer electrochemically active sites with extreme cracks disturbing the efficient transport of Li ions and electrons. Moreover, the coloration efficiency (CE) value, a conventional indicator defining the performance of an EC device, was estimated according to the change in the optical density (OD) related to the transmittance modulation at λ_{633nm} with the applied charge density (Q/A) related to the inserted charge amount per area (same as 3.4 cm^2 for all a-$WO_3 \cdot H_2O$ films), as described below in *Eqs*. (7 and 8) [53]:

$$CE = \Delta OD/(Q/A) \tag{7}$$

$$\Delta OD = \log(T_b/T_c) \tag{8}$$

The CE values are 54.6 cm^2/C for a-$WO_3 \cdot H_2O$/25%, 62.7 cm^2/C for a-$WO_3 \cdot H_2O$/35%, and 50.1 cm^2/C for a-$WO_3 \cdot H_2O$/45%, indicating that a-$WO_3 \cdot H_2O$/35% reveals optimized EC performance. The high CE value of 62.7 cm^2/C in a-$WO_3 \cdot H_2O$/35% is generated by the simultaneous effects of the increased transmittance modulation obtained from the porous film morphology and the rapid switching speeds derived from the efficient charge transport with a high Li ion diffusion rate and good electrical conductivity (see Fig. 4b). In addition, a-$WO_3 \cdot H_2O$/35% showed competitive cycling stability (transmittance retention of 81.95% after 2000-consecutive coloration-bleaching, see Fig. S6a) and the following reasonable reduction of the CV curve area (see Fig. S6b) after the coloration-bleaching processes, which can be induced from the porous morphology to accommodate structure variation during electrochemical reactions.

Fig. 4c presents the specific capacitance (C_{sp}) outcomes of all of the a-$WO_3 \cdot H_2O$ films with stepwise current densities of 2, 4, 6, 8, and 10 A/g according to *Eq*. (9) below [54]:

$$C_{sp} = I/(mdV/dt) \tag{9}$$

At current densities from 2 to 10 A/g, a-$WO_3 \cdot H_2O$/35% exhibits higher specific capacitance compared to the other a-$WO_3 \cdot H_2O$ films, especially 94.2 F/g at 2 A/g with the longest charging/discharging time (see Table S2 and Fig. S4). The higher specific capacitance of a-$WO_3 \cdot H_2O$/35% stems from the increased electrochemical activity with the porous morphology, leading to high levels of the insertion/extraction of Li ions [64,65]. Additionally, a-$WO_3 \cdot H_2O$/35% film shows higher rate capability (specific capacitance retention with increasing current densities from 2 to 10 A/g) of 74.3% when compared at current densities of 2 and 10 A/g, while the a-$WO_3 \cdot H_2O$/25% and a-$WO_3 \cdot H_2O$/45% show lower rate capability outcomes of 54.8% and 27.7% (see Fig. 4c). This improved rate capability is caused by the facilitated electrochemical kinetics resulting from the efficient Li ion and electron transport caused by the porous morphology with the shortened Li ion diffusion length and abundant V_O related to the increased electrical conductivity. To clarify the Li ions and electron transport at a-$WO_3 \cdot H_2O$/35% electrode during an electrochemical reaction, electrochemical impedance spectroscopy (EIS) measurements were conducted in comparison with the a-$WO_3 \cdot H_2O$/25% and a-$WO_3 \cdot H_2O$/45% (see Fig. S5). The a-$WO_3 \cdot H_2O$/35% film shows a smaller semicircle related to the charge transfer resistance and a steep slope of the inclined line related to the ionic diffusion rate compared to a-$WO_3 \cdot H_2O$/25% and a-$WO_3 \cdot H_2O$/45%, demonstrating improved electrical conductivity and a better Li ion diffusion coefficient, respectively, in good agreement with the enhanced flexible EC energy-storage performances [4,55–57].

Fig. 5a shows flexible stability of flexible EC energy-storage devices consisting of a-$WO_3 \cdot H_2O$/35% film, measuring ex-situ performances of transmittance and specific capacitance within the repetitive bending up to 300 cycles with a bending radius of 1.3 cm. As the result, the devices maintained admirable flexible stability (retentions of 74.2% for transmittance modulation and 76.1% for specific capacitance after 300 bending cycles), which can be derived from the stable structure with the optimized V_O defects of a-$WO_3 \cdot H_2O$/35% film. However, the flexible stability of a-$WO_3 \cdot H_2O$ films depending on mechanical deformation could be improved through further studies. Consequently, the flexible a-$WO_3 \cdot H_2O$/35% film including enriched porosity and V_O exhibits outstanding EC performances in transmittance modulation and switching speeds compared to previously reported $WO_3 \cdot H_2O$-based films (see Fig. 5b) [58–63].

In short, with the optimized hydrolysis effects developing porosity and V_O of a-$WO_3 \cdot H_2O$ at a humidity level of 35% during spin-coating and low-temperature annealing, the a-$WO_3 \cdot H_2O$/35% film displays admirable flexible EC energy-storage performances. The improved transmittance modulation and specific capacitance are generated by the accelerated electrochemical activity with the porous film morphology, providing abundant electrochemically active sites. Moreover, the rapid switching speeds and the rate capability stem from the enhanced electrochemical kinetics resulting from the increased electrical conductivity and increased Li ion diffusion coefficient via the abundant V_O and porous morphology, facilitating better charge transport (described in Fig. 4d). For these superior flexible EC energy-storage performances, a-$WO_3 \cdot H_2O$ film with porosity and V_O stemming from the optimized hydrolysis effects at a humidity level of 35% can be suggested for advanced flexible EC energy-storage devices.

4. Conclusion

In sum, we successfully fabricated a-$WO_3 \cdot H_2O$ films with porosity and V_O defects for flexible EC energy-storage devices. The fresh approach presented here to develop porosity and V_O in a-$WO_3 \cdot H_2O$ was realized through a humidity adjustment during the spin-coating and low-temperature annealing processes, leading to the accelerated hydrolysis of $WOCl_4$, which is highly reactive to H_2O. The optimized hydrolysis effects at a humidity level of 35% develop the porous film morphology, deriving from the increased aggregation of amorphous clusters, and abundant V_O generated from the increased intercalation of water molecules. The porous film morphology can provide increased electrochemically active sites and shortened Li ion diffusion pathways. The expanded electrochemically active sites serving as Li ion insertion/extraction sites can lead to the increased Li ion capacity related to the improved transmittance modulation and specific capacitance. Also, the shortened Li ion diffusion pathways can lead to the improved Li ion kinetics, as confirmed from the Li ion diffusion coefficients, which is connecting to the enhanced switching speeds and the specific

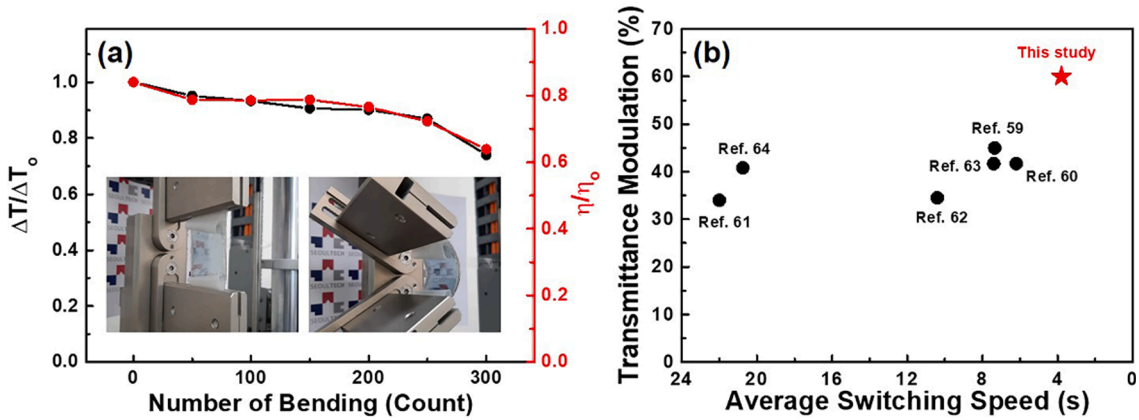

Fig. 5. (a) Retention capability of transmittance modulation at 633 nm and specific capacitance at 1A/g current density in regard to repetitive bending cycles with a bending radius of 1.3 cm (inserted photographs are mechanical bending processes of the flexible solid-state devices) and (b) comparative plot of the transmittance modulation and average switching speeds of coloring and bleaching for a-$WO_3 \cdot H_2O$/35% with previous reported $WO_3 \cdot H_2O$-based films.

capacitance retention with increasing current densities. The abundant V_O can provide extra electrons and efficient charge transport channels, directly affecting the electrical conductivity of the a-$WO_3 \cdot H_2O$ films. The increased electrical conductivity can contribute to the effective supply of the electrons for electrochemical reactions in the films, which is mainly related to the fast switching speeds. Therefore, a-$WO_3 \cdot H_2O$/35% film with the optimized porosity and V_O structures showed superior flexible EC energy-storage performances, including a wide range of transmittance modulation (60.0%), fast switching speeds (3.4 s for the coloration speed and 4.2 s for the bleaching speed), a high CE value (62.7 cm^2/C), and high specific capacitance (94.2F/g at 2 A/g) and good rate capability (74.3%). Also, a-$WO_3 \cdot H_2O$/35% film used as a working electrode to make up a solid-state cell for flexible EC energy-storage device, exhibited admirable flexible stability (retentions of 74.2% for transmittance modulation and 76.1% for specific capacitance after 300 bending cycles).

Thus, the a-$WO_3 \cdot H_2O$ films invented here, fabricated at a low temperature (80 °C) and exhibiting superior flexible EC energy-storage performances, can be a promising candidate for flexible EC energy-storage devices.

CRediT authorship contribution statement

Myeong-Hun Jo: Conceptualization, Methodology, Investigation, Writing - original draft. **Bon-Ryul Koo:** Conceptualization, Methodology, Data curation, Writing - original draft. **Hyo-Jin Ahn:** Conceptualization, Supervision, Writing - review & editing.

Declaration of Competing Interest

The authors declare that they have no known competing financial interests or personal relationships that could have appeared to influence the work reported in this paper.

Acknowledgements

This work was supported by the National Research Foundation of Korea (NRF) grant funded by the Korea government (MSIT) (No. 2019R1 A2 C1005836).

Appendix A. Supplementary material

Supplementary data to this article can be found online at https://doi.org/10.1016/j.apsusc.2021.149664.

References

[1] M.-H. Jo, B.-R. Koo, H.-J. Ahn, Fe co-doping effect on fluorine-doped tin oxide transparent conducting films accelerating electrochromic switching performance, Ceram. Int. 46 (2020) 10578–10584.
[2] G.-H. An, H.-J. Ahn, Excellent electrochemical stability of graphite nanosheet-based interlayer for electric double layer capacitors, Appl. Surf. Sci. 473 (2019) 77–82.
[3] D.-Y. Shin, H.-G. Jo, H.-J. Ahn, Accelerating lithium storage capability of cobalt sulfide encapsulated within anion dual-doped mesoporous carbon nanofibers, Appl. Surf. Sci. 527 (2020), 146895.
[4] K.-H. Kim, S.-J. Jeong, Surface amending effect of N-doped carbon-embedded NiO films for multirole electrochromic energy-storage devices, Appl. Surf. Sci. 537 (2021), 147902.
[5] X. He, X. Li, Y. Chen, X. Xu, X. Gao, Dual-functional electrochromic and energy-storage electrodes based on tungsten trioxide nanostructures, J. Solid State Electrochem. 22 (2018) 2579–2586.
[6] X. Chang, R. Hu, S. Sun, T. Lu, T. Liu, Y. Lei, L. Dong, Y. Yin, Y. Zhu, Efficient synthesis of tungsten oxide hydrate-based nanocomposites for applications in bifunctional electrochromicenergy storage devices, Nanotechnology 29 (2018), 185707.
[7] X. Xia, Z. Ku, D. Zhou, Y. Zhong, Y. Wang, M.J. Huang, J. Tu, H.J. Fan, Perovskite solar cell powered electrochromic batteries for smart windows, Mater. Horiz. 3 (2016) 588–595.
[8] B.-R. Koo, M.-H. Jo, H.-J. Ahn, Multifunctional electrochromic energy storage devices by chemical cross-linking: impact of a $WO_3 \cdot H_2O$ nanoparticle-embedded chitosan thin film on amorphous WO_3 films, NPG Asia Mater. 12 (2020) 10.
[9] H. Li, Y. Lv, X. Zhang, X. Wang, X. Liu, High-performance ITO-free electrochromic films based on bi-functional stacked WO_3/Ag/WO_3 structures, Sol. Energy Mater. Sol. Cells 136 (2015) 86–91.
[10] Y. Ji, Y. Yang, S.-K. Lee, G. Ruan, T.-W. Kim, H. Fei, S.-H. Lee, D.-Y. Kim, J. Yoon, J. M. Tour, Flexible nanoporous WO_{3-x} nonvolatile memory device, ACS Nano 10 (2016) 7598–7603.
[11] G. Cai, J. Wang, P.S. Lee, Next-generation multifunctional electrochromic devices, Acc. Chem. Res. 49 (2016) 1469–1476.
[12] L. Shen, L. Du, S. Tan, Z. Zang, C. Zhao, W. Mai, Flexible electrochromic supercapacitor hybrid electrodes based on tungsten oxide films and silver nanowires, Chem. Commun. 52 (2016) 6296–6299.
[13] G. Cai, X. Cheng, M. Layani, A.W.M. Tan, S. Li, A.L.-S. Eh, D. Gao, S. Magdassi, P. S. Lee, Direct inkjet-patterning of energy efficient flexible electrochromics, Nano Energy 49 (2018) 147–154.
[14] M.-H. Jo, B.-R. Koo, H.-J. Ahn, Accelerating F-doping in transparent conducting F-doped SnO_2 films for electrochromic energy storage devices, Ceram. Int. 46 (2020) 25066–25072.
[15] B.-R. Koo, K.-H. Kim, H.-J. Ahn, Switching electrochromic performance improvement enabled by highly developed mesopores and oxygen vacancy defects of Fe-doped WO_3 films, Appl. Surf. Sci. 453 (2018) 238–244.
[16] G.-H. An, D.-Y. Lee, H.-J. Ahn, Carbon-encapsulated hollow porous vanadium-oxide nanofibers for improved lithium storage properties, ACS Appl. Mater. Interfaces 8 (2016) 19466–19474.
[17] B.-R. Koo, K.-H. Kim, H.-J. Ahn, Novel tunneled phosphorus-doped WO_3 films achieved using ignited red phosphorus for stable and fast switching electrochromic performances, Nanoscale 11 (2019) 3318–3325.
[18] J. Zhu, S. Wei, M.J. Alexander, T.D. Dang, T.C. Ho, Z. Guo, Properties of poly(p-phenylenebenzobisthiazole) thin films embedded with nano-WO_3, Adv. Funct. Mater. 20 (2010) 3076–3084.
[19] Z. Bi, X. Li, Y. Chen, X. He, X. Xu, X. Gao, Large-scale multifunctional electrochromic-energy storage device based on tungsten trioxide monohydrate nanosheets and Prussian White, ACS Appl. Mater. Interfaces 9 (2017) 29872–29880.

[20] Q. Guo, Z. Zhao, Z. Li, D. Wang, G. Nie, A novel solid-state electrochromic supercapacitor with high energy storage capacity and cycle stability based on poly (5-formylindole)/WO_3 honeycombed porous nanocomposites, Chem. Eng. J. 384 (2020), 123370.
[21] J. Zhang, X.L. Wang, X.H. Xia, C.D. Gu, Z.J. Zhao, J.P. Tu, Enhanced electrochromic performance of macroporous WO_3 films formed by anodic oxidation of DC-sputtered tungsten layers, Electrochim. Acta 55 (2010) 6953–6958.
[22] D. Zhou, F. Shi, D. Xie, D.H. Wang, X.H. Xia, X.L. Wang, C.D. Gu, J.P. Tu, Bi-functional Mo-doped WO_3 nanowire array electrochromism-plus electrochemical energy storage, J. Colloid Interface Sci. 465 (2016) 112–120.
[23] J. Huang, C. Tian, J. Wang, J. Liu, Y. Li, Y. Liu, Z. Chen, Fabrication of selective electroless copper plating on PET sheet: effect of PET surface structure on resolution and adhesion of copper coating, Appl. Surf. Sci. 458 (2018) 734–742.
[24] V. Zardetto, T.M. Brown, A. Reale, A.D. Carlo, Substrates for flexible electronics: a practical investigation on the electrical, film flexibility, optical, temperature, and solvent resistance properties, J. Polm. Sci. Pt. B-Polym. Phys. 49 (2011) 638–648.
[25] L. Xiao, Y. Lv, W. Dong, N. Zhang, X. Liu, Dual-functional WO_3 nanocolumns with broadband antireflective and high-performance flexible electrochromic properties, ACS Appl. Mater. Interfaces 8 (2016) 27107–27114.
[26] M. Rakibuddin, A. Mahesh, H. Kim Shinde, Sol-gel fabrication of NiO and NiO/WO_3 based electrochromic device on ITO and flexible substrate, Ceram. Int. 46 (2020) 8631–8639.
[27] U.O. Krasovec, B. Orel, A. Georg, V. Wittwer, The gasochromic properties of sol-gel WO_3 films with sputtered Pt catalyst, Sol. Energy 68 (2000) 541–551.
[28] J.B. Mitchell, N.R. Geise, A.R. Paterson, N.C. Osti, Y. Sun, S. Fleischmann, R. Zhang, L.A. Madsen, M.F. Toney, D.-E. Jiang, A.I. Kolesnikov, E. Mamontov, V. Augustyn, Confined interlayer water promotes structural stability for high-rate electrochemical proton intercalation in tungsten oxide hydrates, ACS Energy Lett. 4 (2019) 2805–2812.
[29] S. Sun, T. Lu, X. Chang, X. Hu, L. Dong, Y. Yin, Flexible electrochromic device based on $WO_3{\cdot}H_2O$ nanoflakes synthesized by a facile sonochemical method, Mater. Lett. 185 (2016) 319–322.
[30] L. Liang, K. Li, C. Xiao, S. Fan, J. Liu, W. Zhang, W. Xu, W. Tong, J. Liao, Y. Zhou, B. Ye, Y. Xie, Vacancy associates-rich ultrathin nanosheets for high performance and flexible nonvolatile memory device, J. Am. Chem. Soc. 137 (2015) 3102–3108.
[31] S.P. Gupta, H.H. Nishad, V.B. Patil, S.D. Chakane, M.A. More, D.J. Late, P.S. Walke, Morphology and crystal structure dependent pseudocapacitor performance of hydrated WO_3 nanostructures, Mater. Adv. 1 (2020) 2492–2500.
[32] N. Zhang, X. Li, Y. Liu, R. Long, M. Li, S. Chen, Z. Qi, C. Wang, L. Song, J. Jiang, Y. Xiong, Defective tungsten oxide hydrate nanosheets for boosting aerobic coupling of amines: synergistic catalysis by oxygen vacancies and Brønsted acid sites, Small 13 (2017) 1701354.
[33] P. Judeinstein, J. Livage, Sol-gel synthesis of WO_3 thin films, J. Mater. Chem. 1 (1991) 621–627.
[34] V.A. Khodzhemirov, V.A. Yevdokimova, V.M. Cherednichenko, Reaction of WCl_6 with alcohols and the activity of the resulting catalysts in polymerization of cyclopentene, Polym. Sci. U.S.S.R. 18 (1976) 581–588.
[35] X.-Y. Tang, M.-F. Li, L.-F. Gao, H. Yan, S.-M. Deng, J.-B. Fan, M.-S. Zheng, S.-L. Deng, Q.-Y. Zhang, S.-Y. Xie, L.-S. Zheng, Facile and high-efficient synthesis of high-performance supercapacitor electrode materials based on the synergistic intercalation and oxidation of layered tungsten disulfide, Adv. Mater. Interfaces 1901122 (2019) 1–8.
[36] Z. Bi, Y. Chen, S. Wang, D. Wang, Hydrolyzed Al(III)-clusters. II: Speciation transformation and stability of Al_{13} aggregates, Colloid Surf. A-Physicochem. Eng. Asp. 440 (2014) 59–62.
[37] Z. Xiao, X. Sun, X. Li, Y. Wang, Z. Wang, B. Zhang, X.L. Li, Z. Shen, L.B. Kong, Y. Huang, Phase transformation of GeO_2 glass to nanocrystals under ambient conditions, Nano Lett. 18 (2018) 3290–3296.
[38] A. Gavrilyuk, U. Tritthart, W. Gey, Photo-stimulated proton-coupled electron transfer in quasi-amorphous WO_3 and MoO_3 thin films, Philos. Mag. 87 (2007) 4519–4553.
[39] J. Huang, X. Xu, C. Gu, M. Yang, M. Yang, J. Liu, Large-scale synthesis of hydrated tungsten oxide 3D architectures by a simple chemical solution route and their gas-sensing properties, J. Mater. Chem. 21 (2011) 13283–13289.
[40] S. Wu, Y. Li, J. Gao, Preparation of tungsten trioxide film with mesoporosity by anodization, Int. J. Nanomanuf. 14 (2018) 259–267.
[41] M. Sun, H. Huang, X. Wei, J. Qiu, Aggregation of MAO coatings and crack formation in the microgrooves on an aluminum surface, Int. J. Electrocehm. Sci. 15 (2020) 839–844.
[42] C. McDonagh, F. Sheridan, T. Butler, B.D. MacCraith, Characterisation of sol-gel-derived silica films, J. Non-Cryst. Solids 194 (1996) 72–77.
[43] B.-R. Koo, H.-J. Ahn, Fast-switching electrochromic properties of mesoporous WO_3 films with oxygen vacancy defects, Nanoscale 9 (2017) 17788–17793.
[44] E. Albanese, C.D. Valentin, G. Pacchioni, H2O adsorption on WO3 and WO3-x (001) surfaces, ACS Appl. Mater. Interfaces 9 (2017) 23212–23221.
[45] R. Zhang, F. Ning, S. Xu, L. Zhou, M. Shao, M. Wei, Oxygen vacancy engineering of WO_3 toward largely enhanced photoelectrochemical water splitting, Electrochim. Acta 274 (2018) 217–223.
[46] G. Ketteler, S. Yamamoto, H. Bluhm, K. Andersson, D.E. Starr, D.F. Ogletree, H. Ogasawara, A. Nilsson, M. Salmeron, The nature of water nucleation sites on TiO_2(110) surfaces revealed by ambient pressure X-ray photoelectron spectroscopy, J. Phys. Chem. C 111 (2007) 8278–8282.
[47] M. Manuja, K.V. Sarath, T. Thomas, J. Jose, G. Jose, K.C. George, Metal insulator transition driven by hydrated water of tungsten trioxide, J. Alloy. Compd. 779 (2019) 15–21.
[48] A.H. Jayatissa, A. Dadi, T. Aoki, Nanocrystalline WO_3 films prepared by two-step annealing, Appl. Surf. Sci. 244 (2005) 453–457.
[49] V.R. Buch, A.K. Chawla, S.K. Rawal, Review on electrochromic property for WO_3 thin films usingdifferent deposition techniques, Mater. Today 3 (2016) 1429–1437.
[50] J. Díaz-Reyes, R. Castillo-Ojeda, M. Galván-Arellano, O. Zaca-Moran, Characterization of WO_3 thin films grown on Silicon by HFMOD, Adv. Condens. Matter Phys. 2013 (2013) 9.
[51] J. Wang, Z. Wang, B. Huang, Y. Ma, Y. Liu, X. Qin, X. Zhang, Y. Dai, Oxygen vacancy induced band-gap narrowing and enhanced visible light photocatalytic activity of ZnO, ACS Appl. Mater. Interfaces 4 (2012) 4024–4030.
[52] Z. Wang, J. Su, H. Qi, P. Pan, M. Jiang, Porous nanocrystalline WO_3 thin films: fabrication, electrical and optical properties, Surf. Innov. (2020) 1–8.
[53] K.-H. Kim, B.-R. Koo, H.-J. Ahn, Sheet resistance dependence of fluorine-doped tin oxide films for highperformance electrochromic devices, Ceram. Int. 44 (2018) 9408–9413.
[54] J. Li, W. Zhao, F. Huang, A. Manivannan, N. Wu, Single-crystalline $Ni(OH)_2$ and NiO nanoplatelet arrays as supercapacitor electrodes, Nanoscale 3 (2011) 5103–5109.
[55] D. Xiong, X. Li, H. Shan, B. Yan, L. Dong, Y. Cao, D. Li, Controllable oxygenic functional groups of metalfree cathodes for high performance lithium ion batteries, J. Mater. Chem. A 3 (2015) 11376–11386.
[56] G.-H. An, J.I. Sohn, H.-J. Ahn, Hierarchical architecture of hybrid carbonencapsulated hollow manganese oxide nanotubes with a porous-wall structure for high-performance electrochemical energy storage, J. Mater. Chem. A 4 (2016) 2049–2054.
[57] G.-H. An, H.-J. Ahn, Ultrafast lithium storage of high dispersed silicon and titanium oxide nanoparticles in carbon, J. Alloy. Compd. 710 (2017) 274–280.
[58] C.Y. Ng, K.A. Razak, Z. Lockman, Effect of annealing on acid-treated $WO_3{\cdot}H_2O$ nanoplates and their electrochromic properties, Electrochim. Acta 178 (2015) 673–681.
[59] L. Liang, J. Zhang, Y. Zhou, J. Xie, X. Zhang, M. Guan, B. Pan, Y. Xie, High-performance flexible electrochromic device based on facile semiconductor-to-metal transition realized by $WO_3{\cdot}2H_2O$ ultrathin nanosheets, Sci Rep 3 (2013) 1–8.
[60] Y. Yue, H. Li, K. Li, J. Wang, H. Wang, Q. Zhang, Y. Li, P. Chen, High-performance complementary electrochromic device based on $WO_3{\cdot}0.33H_2O$/PEDOT and prussian blue electrodes, J. Phys. Chem. Solids 110 (2017) 284–289.
[61] H. Li, J. Wang, Q. Shi, M. Zhang, C. Hou, G. Shi, H. Wang, Q. Zhang, Y. Li, Q. Chi, Constructing three-dimensional quasi-vertical nanosheet architectures from self-assemble two-dimensional $WO_3{\cdot}2H_2O$ for efficient electrochromic devices, Appl. Surf. Sci. 380 (2016) 281–287.
[62] H. Qu, X. Zhang, H. Zhang, Y. Tian, N. Li, H. Lv, S. Hou, X. Li, J. Zhao, Y. Li, Highly robust and flexible $WO_3{\cdot}2H_2O$/PEDOT films for improved electrochromic performance in near-infrared region, Sol. Energy Mater. Sol. Cells 163 (2017) 23–30.
[63] H. Li, G. Shi, H. Wang, Q. Zhang, Y. Li, Self-seeded growth of nest-like hydrated tungsten trioxide film directly on FTO substrate for highly enhanced electrochromic performance, J. Mater. Chem. A 2 (2014) 11305–11310.
[64] J. Zhang, J. Yang, G. Leftheriotis, H. Huang, Y. Xia, C. Liang, Y. Gan, W. Zhang, Integrated photo-chargeable electrochromic energy-storage devices, Electrochim. Acta 345 (2020), 136235.
[65] D. Zhang, B. Sun, H. Huang, Y. Gan, Y. Xia, C. Liang, W. Zhang, J. Zhang, A solar-driven flexible electrochromic supercapacitor, Materials 13 (2020) 1206.